communications earth & environment

Article

https://doi.org/10.1038/s43247-024-01644-9

Robust future projections of global spatial distribution of major tropical cyclones and sea level pressure gradients

Hiroyuki Murakami [1] ✉, William F. Cooke [1], Ryo Mizuta[2], Hirokazu Endo[2], Kohei Yoshida [2], Shuai Wang [3] & Pang-Chi Hsu [4] ✉

Despite the profound societal impacts of intense tropical cyclones (TCs), prediction of future changes in their regional occurrence remains challenging owing to climate model limitations and to the infrequent occurrence of such TCs. Here we reveal projected changes in the frequency of major TC occurrence (i.e., maximum sustained wind speed: ≥ 50 m s^{-1}) on the regional scale. Two independent high-resolution climate models projected similar changes in major TC occurrence. Their spatial patterns highlight an increase in the Central Pacific and a reduction in occurrence in the Southern Hemisphere—likely attributable to anthropogenic climate change. Furthermore, this study suggests that major TCs can modify large-scale sea-level pressure fields, potentially leading to the abrupt onset of strong wind speeds even when the storm centers are thousands of kilometers away. This study highlights the amplified risk of storm-related hazards, specifically in the Central Pacific, even when major TCs are far from the populated regions.

Tropical cyclones (TCs) can cause substantial economic losses and high numbers of fatalities and therefore changes in the frequency of TC occurrence are of great societal interest and importance. In the United States, 387 billion-dollar natural disaster events have been reported since 1980, accounting for total economic losses of $2.74 trillion and 16,434 fatalities[1]. Among them, TC-related natural disasters accounted for approximately 52% of the total economic losses and 42% of the total number of fatalities[1]. Moreover, among the TC-related damages, approximately 84% of the related economic losses and 91% of the related fatalities were caused by major TCs[1], defined as TCs with lifetime maximum sustained wind speed of ≥50 m s^{-1}, which is equivalent to Category 3–5 hurricanes according to the Saffir-Simpson's hurricane scale[2]. The substantial societal impact of major TCs is also of global importance. For example, among the top five deadliest worldwide natural disasters since 1970, three were major TC events: Cyclone Bhola in 1970, Cyclone Gorky in 1991, and Cyclone Nargis in 2008[3]. Given the substantial impact of major TCs on society, it is important to identify the global regions where the occurrence of major TCs and the scale of their impact might increase in the future owing to anthropogenic climate change[4–6].

Addressing possible future changes in the regional occurrence of major TCs remains a challenge for the science community for several reasons. First, the horizontal resolution employed in most global dynamical models is coarser than 50 km, which is insufficient to simulate and resolve major TCs[7,8]. Second, it is difficult to isolate the effect of anthropogenic forcing from internally generated noise, especially for major TCs because of the rarity of such events[9]. Third, there are substantial variations in projections of regional TC occurrence among climate models, which makes it difficult to derive robust future projections[10–12]. Although recent studies reported that some high-resolution dynamical global models could simulate major TCs[8,13–16], conducting multidecade simulations with multiple ensemble members remains challenging owing to the limited availability of computational resources[9]. Moreover, even for climate models with the same high level of horizontal resolution, different physical schemes could lead to variation in future projections of TCs[17], resulting in diverse results of regional TC projections[18–21].

To tackle those challenges, the High-Resolution Model Intercomparison Project (HighResMIP) was launched as part of the Coupled Model Intercomparison Project Phase 6[22–24]. This project evaluated and compared simulations and projections of TCs among multiple high-resolution climate models with horizontal resolution in the range 25–250 km[22–24]. Although the intercomparison project is useful in identifying confidence and uncertainty in future projections, ref. 23. reported that

[1]National Oceanic and Atmospheric Administration/Geophysical Fluid Dynamics Laboratory, Princeton, NJ, USA. [2]Meteorological Research Institute, Tsukuba, Ibaraki, Japan. [3]Department of Geography and Spatial Sciences, University of Delaware, Newark, DE, USA. [4]Key Laboratory of Meteorological Disaster of Ministry of Education/Collaborative Innovation Center on Forecast and Evaluation of Meteorological Disasters, Nanjing University of Information Science and Technology, Nanjing, China. ✉e-mail: hir.murakami@gmail.com; pangchi.hsu@gmail.com

only two HighResMIP models (i.e., the Centre National de Recherches Météorologiques's CNRM-CM6-1 model[25] and the Euro-Mediterranean Centre on Climate Change's CMCC-CM2-VHR4 model[26]) could simulate major TCs but with substantial biases. It is found that these two HighResMIP models markedly underestimate the global frequency of major TC occurrence relative to observations (Supplementary Fig. 1), revealing that assessment of regional changes in major TCs remains challenging, even in the HighResMIP project.

Meanwhile, an increased occurrence of major TCs in a specific region can directly cause hazards such as strong winds, heavy rainfall, flooding, and storm surges, but also indirectly influence remote hydroclimatological processes via the advection of moist air, even though the storm center might be located far from the affected regions[27]. However, the full extent of the remote effects of major TCs, beyond that of heavy rainfall associated with moisture advection, requires a more comprehensive understanding. For example, Lahaina, located leeward of the mountains on Maui Island in Hawaii, experienced a catastrophic wildfire in August 2023. This wildfire occurred because of the abrupt onset of strong, dry easterly winds that developed rapidly within a period of several hours on August 8, 2023. The scientific community argued that abrupt intensification of the surface pressure gradient was the main reason for the sudden development of strong winds[28]. The concurrent occurrence of a high-pressure system to the north of Maui and the low-pressure system to the south of Maui associated with Hurricane Dora, which propagated westward approximately 1100 miles south of Maui at Category 4 intensity (maximum sustained wind speed: $\geq 58\ m\ s^{-1}$), generated an abrupt rise in the meridional surface pressure gradient centered around Maui[28]. Although the strength of the pressure gradient appeared largely associated with the low-pressure system of Hurricane Dora, it is unclear to what extent Hurricane Dora contributed to the development of the high-pressure system to the north of Lahaina.

Based on this background, this study aims to identify future changes in the regional frequency of major TC occurrence using two independent dynamical models that have been illustrated in this study to accurately reproduce major TCs in present-day climate simulations (Supplementary Fig. 1)[13,29,30]. Another objective is to quantify the extent to which major TCs can influence large-scale pressure fields and potentially trigger the abrupt onset of strong winds remotely. This study reveals a consistent spatial pattern of future changes in the frequency of major TC occurrences across the models, notably showing marked increases in the Central Pacific, including Hawaii. Moreover, this study finds that major TCs can alter large-scale sea level pressure fields, leading to sudden changes in sea level pressure gradient and potentially causing strong winds to occur abruptly, even though the storm center is far from the affected areas. With the projected rise in major TC occurrences near Hawaii, wildfire disasters similar to the one associated with Hurricane Dora in 2023 are expected to escalate in the future. Detailed results are elaborated in the subsequent sections.

Results

Robust future changes in major tropical cyclones

Despite the challenges in simulating major TCs using global dynamical models, two other independent high-resolution global models can reasonably simulate the frequency of major TC occurrence globally (Supplementary Fig. 1). These models are the high-resolution version of the Seamless System for Prediction and Earth System Research (SPEAR_HI)[9,29,30] developed at the National Oceanic and Atmospheric Administration (NOAA) Geophysical Fluid Dynamics Laboratory (GFDL), and the high-resolution Meteorological Research Institute (MRI, Japan) atmospheric general circulation model (AGCM) version 3.2 (MRI-AGCM3.2S)[13,31,32] (see Methods).

After conducting consecutive historical and future projections, the two independent models project robust spatial patterns of the changes in the frequency of major TC occurrence globally (Fig. 1, see "Methods" section). Specifically, they consistently project an increase in major TC occurrence in the Central Pacific region near Hawaii and the eastern/northern North Atlantic and a reduction in major TC occurrence in the Southern Hemisphere, the westernmost portion of the tropical western North Pacific, Gulf of Mexico, and Caribbean Sea. Although regional change varies slightly between the two models, they generally project an increase in the occurrence of major TC near California, Northeast Asia (e.g., Japan, Korea, and Northeast China), the northeast coast of Canada, and East Africa near Mozambique. Additionally, they generally project poleward shifts in the spatial extent of major TC occurrence in both hemispheres, albeit with a smaller shift in the Southern Hemisphere than in the Northern Hemisphere.

Figure 2 displays the simulated and observed temporal evolution of the number of major TCs and major storm days (see "Methods" section). The simulations with SPEAR_HI, including expected changes in anthropogenic forcing such as greenhouse gases and aerosols (SPEAR_HI_ALL, red curves), show a statistically significant reduction in the global number of major TCs toward the end of the 21st century. The magnitude of the projected reduction is approximately 13.6% during 2021–2061 and 23.1% during 2061–2100, relative to the climatology during 1981–2020 (Fig. 2a). Although the change projected by MRI-AGCM3.2S (purple curves) is smaller than that projected by SPEAR_HI, MRI-AGCM3.2S also projects a statistically significant reduction in the global number of major TCs by approximately 9.5% by the end of the 21st century. Specifically, both models project a greater reduction in the Southern Hemisphere (Fig. 2c) than in the Northern Hemisphere (Fig. 2b). Moreover, both models robustly project a statistically significant increase in the number of major TCs in the central Pacific (0°–90°N, 140°–180°W) by approximately 130%–180% by the end of the 21st century (Fig. 2d). There are no statistically significant changes evident in the SPEAR_HI experiments in which changes in anthropogenic forcing are not considered (SPEAR_HI_NAT, blue curves), indicating the marked influence of anthropogenic forcing on the projected changes in major TCs. It should be noted that SPEAR_HI_ALL projects statistically significant changes in the number of major TCs even during the near-future period (2021–2060), whereas MRI-AGCM3.2S does not (Fig. 2a–d). This discrepancy could arise because MRI-AGCM3.2S employs only a single member such that internal variability obscures the effect of anthropogenic forcing on the changes in major TCs, whereas SPEAR_HI_ALL employs a 10-member ensemble that effectively filters out the effect of internal variability.

We further assessed the projected changes in major TC days (Fig. 2e–h). The variable of major TC days considers the number of major TCs and the duration of TCs at major TC intensity, representing the summation of Fig. 1 within a specific domain. Unlike the notable reductions observed in the global number of major TCs (Fig. 2a), the number of global major TC days does not show a statistically significant reduction in either model (Fig. 2e). The discrepancy in the degree of future changes between the number of major TCs and the number of major TC days is more pronounced in the Northern Hemisphere than in the Southern Hemisphere (Fig. 2b–g). Moreover, both models robustly project statistically significant increases in the number of major TC days in the central Pacific at the end of the 21st century (Fig. 2h). These results underscore the substantial increase in the risk of major TCs and associated hazards near Hawaii in the future.

Despite a decrease in major TC genesis frequency, increases or persistence in major storm days can be attributed to projected increases in the mean duration of storms at major TC intensity. Supplementary Fig. 2 illustrates projected increases in mean duration at major TC intensity across all ocean basins. Additionally, we conducted a principal component analysis[33] to quantify each factor (i.e., genesis, tracks, and the nonlinear combinations) to the total changes in the major TC days projected by the SPEAR_HI for each domain, as depicted in Supplementary Fig. 3. The results reveal that in the global, Northern Hemisphere, and Southern Hemisphere regions, decreases in TC genesis largely contribute to the reductions in major TC days. However, these reductions are offset by the track effect, which represents increases in the mean duration of storms at major TC intensity. The Central Pacific is the only region where both increases in TC genesis and longer storm durations at major TC intensity contribute to the increase in major TC storm days.

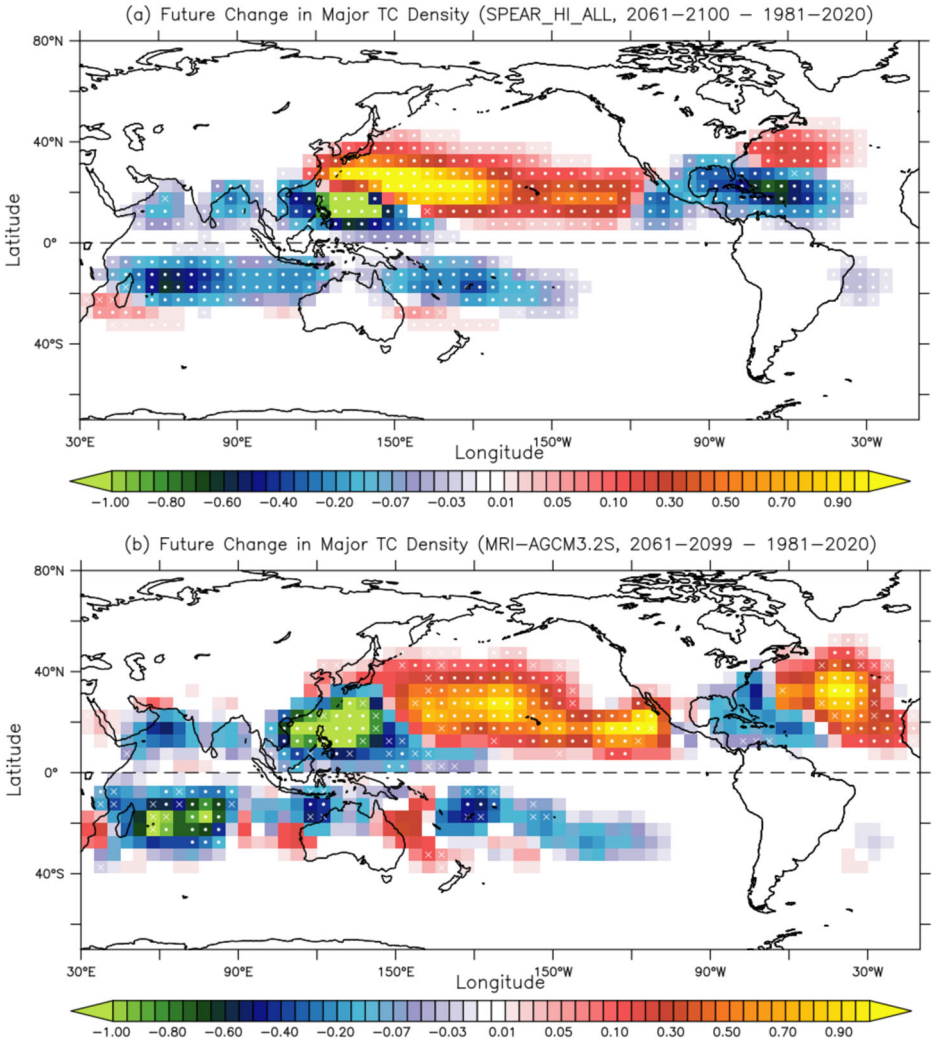

Fig. 1 | Projected future changes in the frequency of major TC occurrence. a SPEAR_HI. **b** MRI-AGCM3.2S. Differences in the ensemble mean of the future (2061–2100) relative to the present-day (1981–2020) are shown in (**a**), In (**b**), differences in the mean of 2061–2099 relative to the mean of 1981–2020 are shown based on the available simulation outputs that end in 2099 for MRI-AGCM3.2S (see "Methods" section). A white dot (cross mark) indicates that the future change over the grid cell is statistically significant at the 99% (95%) level according to a bootstrap significance test (units: number per year per 5° × 5° grid box).

Abrupt increase in sea level pressure gradient by major TCs

To better understand the potential effect of Hurricane Dora on the generation of the surface pressure gradient near Maui, we developed composite maps by averaging the simulated storm events where simulated major TCs were positioned approximately 1000 km south of Maui, to mimic the relative positions of major hurricanes after Hurricane Dora. Figure 3a–c displays simulated mean composites of 6-hourly sea level pressure (SLP) anomalies based on the locations of major TCs simulated by SPEAR_HI. To remove the background influence, the anomaly in 6-hourly SLP was computed by subtracting the climatological multiyear 6-hourly mean derived from the preceding 20 years relative to the target time (see "Methods" section). When the centers of simulated major TCs are positioned south of Lahaina (0°–15°N, 160°–155°W; Fig. 3b; Supplementary Fig. 4 provides a close-up of the area near Hawaii), a notable reduction in SLP is observed to the south, as expected, corresponding to the minimum SLP associated with the simulated major TCs. More importantly, positive SLP anomalies of approximately 0.5 hPa are evident to the north and northeast of the Hawaii Islands. Previous case studies have reported that the generation of positive SLP anomalies north of a TC center can be caused by the advection of lower potential vorticity from lower latitudes via the primary TC circulation[34,35]. Such a pair of negative and positive SLP anomalies could cause a strong meridional SLP gradient around Hawaii, leading to abrupt intensification of easterly winds, such as that associated with Hurricane Dora.

To confirm that major TCs can generate a pair of SLP anomalies, we produced similar composites for major TCs in different locations (Fig. 3a, c), which consistently show pairs of SLP anomalies around major TCs. Because MRI-AGCM3.2S cannot provide an adequate sample size of major TCs near Hawaii owing to it being a single-member ensemble, we developed composites for all TCs regardless of intensity and obtained a similar pair of SLP anomalies (Fig. 3d–f). It should be noted that the composite wind structure is not axisymmetric but is rather elongated in the meridional direction (shadings in Fig. 3). Although the strong SLP gradients are mostly attributed to the lower SLP anomalies associated with major TCs, the generation of positive SLP anomalies also plays a crucial role in enhancing the strong SLP gradient.

Positive and negative SLP anomalies associated with TCs can occur globally (Supplementary Figs. 5 and 6), and it should be noted that positive SLP anomalies can be observed to the south or southeast of the TC centers in the Southern Hemisphere owing to the clockwise direction of the primary circulation of such TCs (Supplementary Fig. 6). Moreover, the occurrence of positive SLP anomalies is not only specific to the model simulations. Still, it is evident in reanalysis datasets (Supplementary Figs. 5c, d, 6c, d).

Future changes in extreme rises in sea level pressure gradient

Considering the projected increase in the frequency of occurrence of major TC near Hawaii (Fig. 2h), a corresponding increase in the frequency of extreme rises in the SLP gradient is also expected. To quantify the increase, the tendency of the SLP meridional gradient (TSLPG; see "Methods" section) was computed. A larger value of the TSLPG indicates abrupt development of the SLP meridional gradient within 24 h. Focusing on the frequency of extreme TSLPG events near Hawaii, TSLPG was computed for every 6 h during summer (July–October), and extreme events were

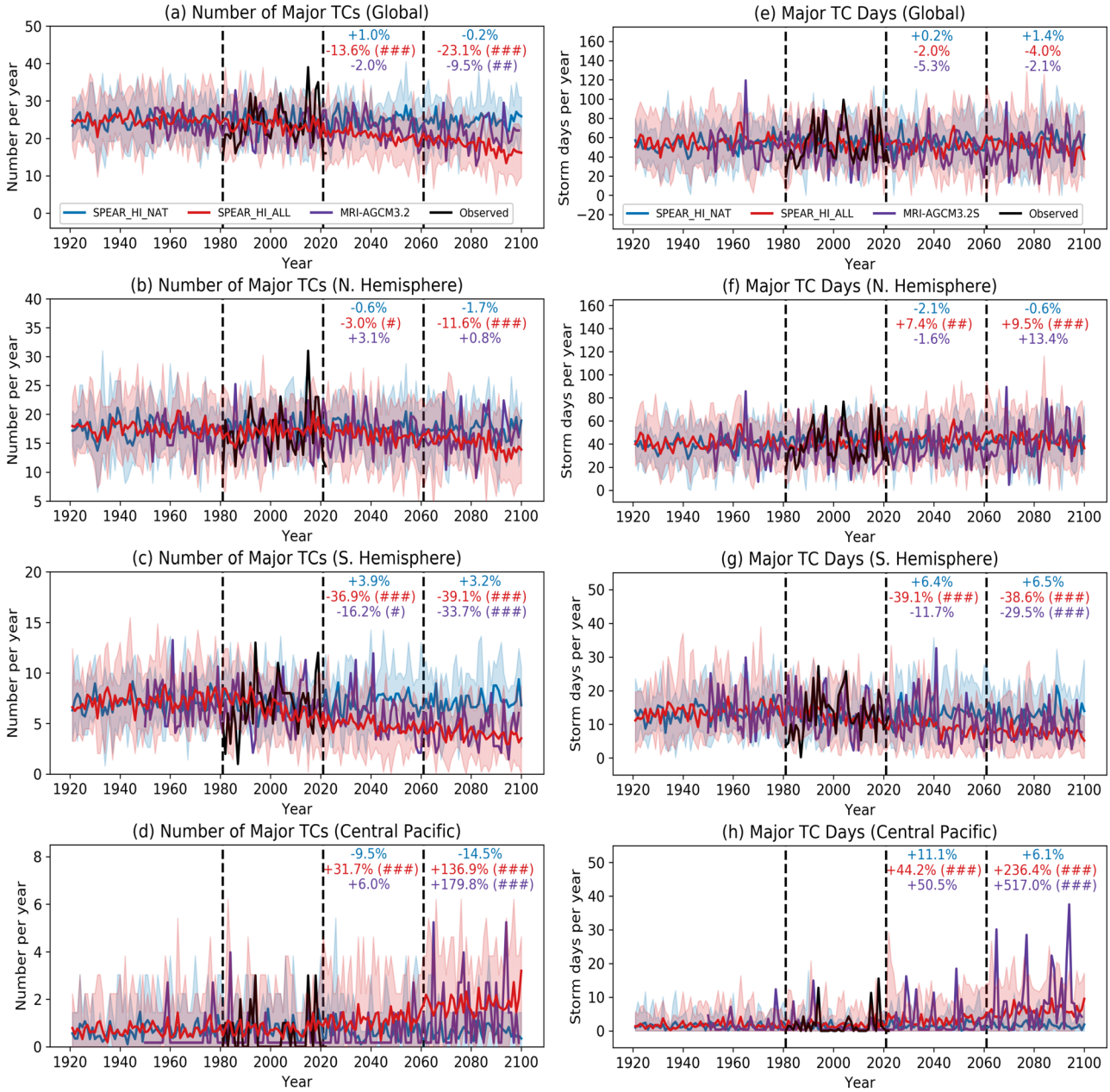

Fig. 2 | Time series of simulated and observed major TC number and storm days. **a** Number of global major TCs (unit: number per year) observed (black), simulated by the SPEAR_HI_ALL large-ensemble experiments (red), SPEAR_HI_NAT large-ensemble experiments (blue), and MRI-AGCM3.2S (purple). Shading indicates the minimum and maximum ranges among the ensemble members by SPEAR_HI. Numbers in the panel denote fractional changes for 2021–2060 and 2061–2100 (2061–2099 for MRI-AGCM3.2S) relative to the mean of 1981–2020. Based on a bootstrap significance test, the triple, double, and single hashes indicate that the projected change is statistically significant at the 99%, 95%, and 90% levels, respectively. **b**–**d** As in (**a**), but for the Northern Hemisphere, Southern Hemisphere, and Central Pacific (0°–90°N, 140°–180°W), respectively. **e**–**h** As in (**a**–**d**), respectively, but for major TC storm days. Major TC numbers are calculated as the total number of TCs with maximum sustained wind speed that exceeded 50 m s^{-1} as the lifetime maximum intensity, whereas major TC storm days are calculated as the total number of days on which TCs record major TC intensity (i.e., maximum sustained wind speed: ≥50 m s^{-1}).

identified by collecting those events exceeding various percentile thresholds (e.g., 90th, 95th, 99th, 99.5th, 99.9th, 99.95th, and 99.99th percentiles; see "Methods" section).

Figure 4 displays the average frequency of extreme TSLPG events for each 40-year period for each percentile threshold. SPEAR_HI projects statistically significant increases in extreme events from the 90th to the 99.9th percentile thresholds for both the near-future period (2021–2060) and the end of the 21st century (2061–2100). Additionally, SPEAR_HI projects a statistically significant increase in the rate of 99.95th percentile events for the end of the 21st century, relative to present-day decades (1981–2020) (Fig. 4a). Although MRI-AGCM3.2S generally projects similar changes, it does not project statistically significant increases in the near-future period, probably because of internal variability. Overall, the robust increases in extreme TSLPG events near Hawaii suggest a heightened occurrence of sudden onset of strong wind speeds and associated increases in the occurrence of TC-related hazards, such as the wildfire associated with Hurricane Dora in 2023.

We extended the TSLPG analysis to the global domain by applying calculations similar to those used for Hawaii to each grid cell globally (see Methods). The projected changes in the frequency of extreme TSLPG events at the 99.95th percentile threshold by SPEAR_HI and by MRI-AGCM3.2S are presented in Supplementary Fig. 7a, b, respectively. Both models project

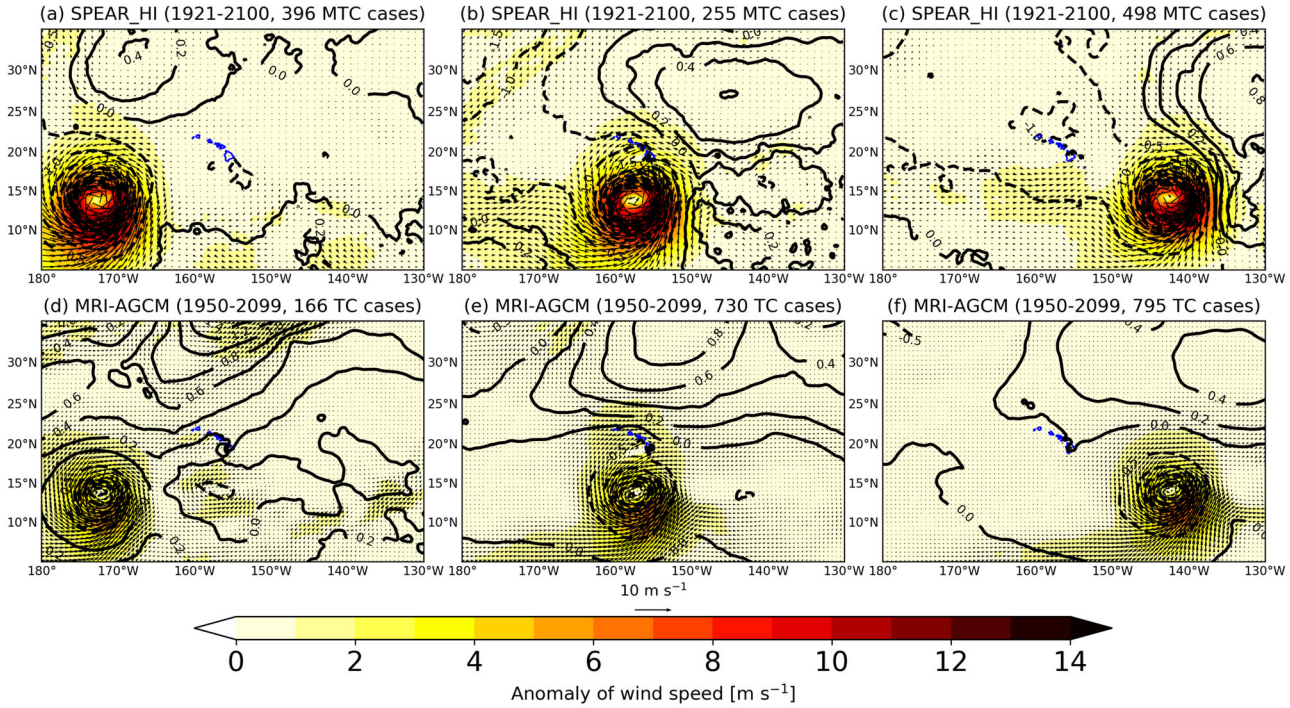

Fig. 3 | Composite structure of SLP and wind anomalies. Composite of 6-hourly anomalies of SLP and zonal and meridional wind components when the centers of storms with major TC intensity (i.e., maximum sustained wind speed: ≥50 m s^{-1}) are located over (**a**) the southwest Hawaiian region 0°–15°N, 180°–170°W, **b** the southern Hawaiian region 0°–15°N, 160°–155°W, and **c** the southeastern Hawaiian region 0°–15°N, 145°–140°W using the 30-member SPEAR_HI_ALL large-ensemble simulations over the period 1921–2100. Numbers represented in the title of each panel denote the sample sizes used for the composites. **d**–**f** As in (**a**–**c**), respectively, but for the MRI-AGCM3.2S experiment for 1950–2099 when simulated TCs with named storm intensity (i.e., maximum sustained wind speed: ≥17.5 m s^{-1}) are in each region. Contours denote SLP anomalies (hPa). Solid (dashed) contours denote positive (negative) values of SLP anomalies. The contour interval is 0.5 hPa for negative values and 0.2 hPa for positive values. Vectors denote anomalies of wind vectors. Shadings denote anomalies of wind speed (unit: m s^{-1}).

similar spatial patterns of changes except in the equatorial areas, showing increases in the central Pacific, including the Hawaii region, and reductions in the western portion of the western North Pacific, Gulf of Mexico, Caribbean Sea, and broad open oceans in the Southern Hemisphere. Extreme TSLPG events do not always accompany TC activity near the equator, mid-latitudes, and high latitudes. To filter out the effect of non-TC events, Fig. 5a, b show the same information as in Supplementary Fig. 7a, b, respectively, but for extreme events at the 99.95th percentile threshold only when any TCs (maximum sustained wind speeds: ≥17.5 m s^{-1}) exist over the grid cells during these extreme events. Both SPEAR_HI and MRI-AGCM3.2S project robust spatial patterns of change in TC-related extreme TSLPG events, revealing increasing occurrence in the Central Pacific and diminishing occurrences in the Gulf of Mexico, Caribbean Sea, and broad open oceans in the Southern Hemisphere (Fig. 5a, b). Similar results were obtained for other percentile thresholds, e.g., the 99.5th percentile events (Supplementary Fig. 8). These spatial patterns resemble the projected changes in the frequency of major TC occurrence (Fig. 1a, b), underscoring the critical role of changes in major TCs occurrence in the changes in extreme rises in the SLP gradient.

Overall, these findings underscore the far-reaching effects of TCs on extreme weather phenomena such as intense winds and wildfires. It is important to quantify both the local and remote effects associated with changes in the frequency of major TC occurrence to estimate accurately the projected changes in the potential risk of TC-related hazards.

Summary and discussion

We showed that the two independent high-resolution global climate models can project robust future changes in the spatial patterns of the frequency of major TC occurrence attributable to increased anthropogenic forcing. These changes comprise increased frequency in the Central Pacific, including the Hawaii region, northeastern Canada, and Northeast Asia, and reduced frequency in the western quadrant of the tropical western North Pacific, Gulf of Mexico, Caribbean Sea, and broad open oceans in the Southern Hemisphere. Moreover, the two models also robustly project poleward shifts in the spatial extent of major TC occurrence in both hemispheres. The projected increase in the frequency of major TC occurrence would also lead to the increased frequency of extreme rises in the SLP meridional gradient within 24 h. Specifically, the projected increase in frequency of major TC occurrence near Hawaii would lead to more frequent extreme rises in SLP meridional gradient there, potentially leading to increased frequency of sudden onset of strong winds and possible wildfire events, as seen during Hurricane Dora in 2023.

This study underscores that TC hazards can impact residential regions even though a major TC is thousands of kilometers away. This highlights the importance of maintaining preparedness for potential damage from major TCs, regardless of their distance from populated areas. This study projects increases in abrupt rises in SLP gradients in certain coastal areas, which could lead to more frequent sudden onset of strong winds and wildfires. Moreover, these abrupt rises in SLP gradients may bring strong winds accompanied by substantial moisture, resulting in the sudden onset of heavy rainfall. Notably, a recent study has documented an increasing frequency of extreme rainfall events over western Japan over the past 40 years, which could be linked to more frequent occurrences of major TCs over the open ocean southwest of Japan[27].

Some caveats are noted in relation to the results. This study considered only two models for the evaluation of future changes. Evaluation using additional models will be important to enhance confidence in the reported projections, although the availability of other global models capable of producing reliable simulations of major TCs is currently limited. Generally, previous model intercomparison projects reported variation in regional

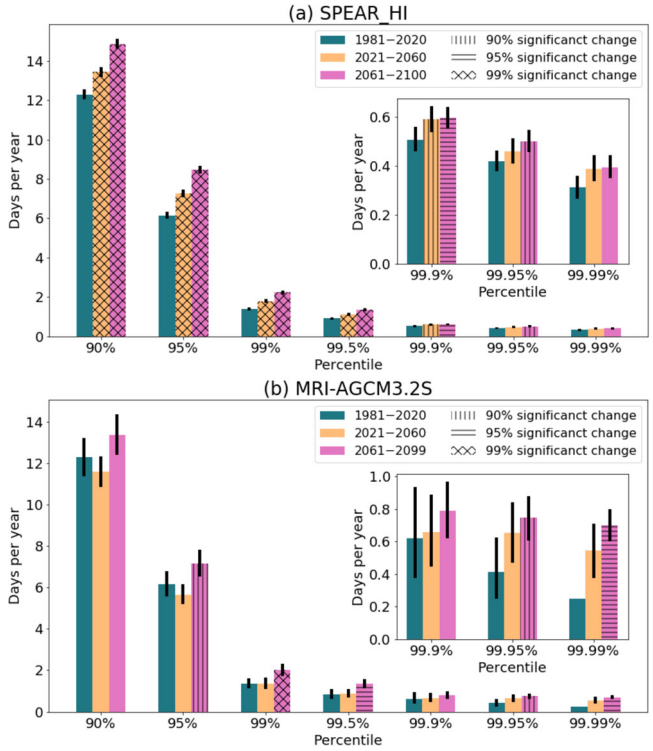

Fig. 4 | Simulated frequency of extreme events of abrupt increases in SLP gradient near Hawaii. Extreme TSLPG events were calculated for each percentile threshold (i.e., 90th, 95th, 99th, 99.5th, 99.99th, 99.95th, and 99.99th percentiles). **a** SPEAR_HI_ALL. **b** As in (**a**), but for MRI-AGCM3.2S. Green, orange, and pink bars denote the simulated frequency of extreme TSLPG events during the present-day decades (1981–2020), near-future decades (2021–2060), and decades at the end of the 21st century (2061–2100 for SPEAR_HI and 2061–2099 for MRI-AGCM3.2S), respectively. Error bars denote 95% confidence intervals calculated using a bootstrap method. Based on a bootstrap significance test, the triple, double, and single hashes indicate that the future change is statistically significant at 99%, 95%, and 90% confidence levels, respectively, relative to the mean of present-day decades. The results for the 99.9th, 99.95th, and 99.99th cases are rescaled in the embedded panels.

projections of TC occurrence among the different climate models[10–12]. These intercomparisons, however, have not explicitly addressed the extent to which underlying model biases might influence future projections. It is important to stress that model biases in terms of the frequency of major TC occurrence in the present-day climate can substantially impact future projections[19]. For example, if a model critically underestimates the frequency of major TC occurrence in a specific region in a present-day climate simulation, the model is unlikely to project a reduction in major TC occurrence in that region because of the inherent lack of recognition of major TC occurrence in that area. Therefore, before a multimodel ensemble approach is adopted for future projections, selecting models based on their performance in simulating the present-day climate is important[19].

The findings of our study also highlight the importance of the two-way interaction between TCs and their surrounding environment. One such interaction that is commonly overlooked is the modified SLP anomaly associated with the remote existence of a TC, which can be an important element affecting TC hazards. Although several statistical-downscaling studies have estimated TC hazards and associated risk[36–38], they have mainly focused on the effect of large-scale environment on TCs and have not considered the reciprocal effect of TCs on the environment, such as the remote increase in SLP induced by the presence of TCs. Therefore, there is potential for statistical–dynamical models to underestimate the full nature of the effect of TCs on TC-related hazards.

It is also noted that the future emission scenarios considered in this study represent a high-emission scenario (i.e., Shared Socioeconomic Pathway 5–8.5 for SPEAR_HI and Representative Concentration Pathway 8.5 for MRI-AGCM3.2S). SPEAR_HI and MRI-AGCM3.2S project a rise in global mean surface temperature of approximately 3.5 and 3.2 K, respectively, by the end of the 21st century, relative to present-day decades. It is expected that under different mitigated emission scenarios, the degree of future changes in major TCs revealed in this study would be smaller. Our findings, however, emphasize the distinct climatic changes in major TCs under high-emission scenarios that differ substantially from SPEAR_HI_NAT, where fixed levels of anthropogenic forcing were assumed.

Overall, our study underscores the importance of identifying possible regional changes in major TCs and their associated hazards. We recognize the need for continued refinement of the resolution and physics of numerical models to enhance our understanding of the complex interactions between TCs and the environment and to elucidate their implications regarding future TC-related hazards.

Methods

Observed datasets

We used 6-hourly surface wind speeds and SLP from the two reanalysis datasets: the Japanese 55-year Reanalysis (JRA-55, 1.25° × 1.25°, 1958–2022)[39] and NCEP Climate Forecast System (CFSR, 0.5° × 0.5°, 1979–2022)[40].

For observed TC data, we utilized the International Best Track Archive for Climate Stewardship version 4 (IBTrACS, 1981–2022)[41]. The positions of major TCs were identified at 6-hourly intervals when TC intensity exceeded the major TC threshold (i.e., maximum sustained wind speed: ≥50 m s^{-1}). We counted the frequency of major TC occurrence within each 5° × 5° grid box. The sum of the counts for each grid box was defined as the frequency of major TC occurrence (or major TC density). We applied a smoothing technique to the major TC density fields. The smoothing was applied using a nine-point moving average in which the weights were assigned based on the distance from the center of each grid box. Dividing the total frequency of major TC occurrence by four provided the number of major TC storm days.

Models

We utilized the Geophysical Fluid Dynamics Laboratory (GFDL) high-resolution version of the Seamless System for Prediction and Earth System Research, known as SPEAR_HI[9,29,30]. SPEAR with medium resolution (SPEAR_MED)[9,29] is a coupled atmosphere–ocean dynamical model used for the experimental operational seasonal to decadal prediction model developed at GFDL. SPEAR comprises a coupled atmospheric–oceanic model consisting of the AM4-LM4 atmosphere and land-surface model[42,43], the MOM6 ocean model (https://github.com/NOAA-GFDL/MOM6), and the SIS2 sea ice model.

Whilst SPEAR_MED employs a 50-km mesh for the atmospheric and land components and a 100-km mesh for the sea ice and oceanic components, SPEAR_HI employs a 25-km mesh for atmospheric and land components and the same resolution as that used for the sea ice and oceanic components by SPEAR_MED. Additionally, SPEAR_HI incorporates specific model tuning parameters designed to optimize TC simulations[30].

We also utilized the 20-km-mesh Meteorological Research Institute (MRI) atmospheric general circulation model, MRI-AGCM3.2S[13,31,32], which is an atmosphere-only model. A detailed description of this model can be found in refs. 13,31,32. Note that the updated cumulus convection scheme developed by ref. 44. substantially improved the model's ability to simulate major TCs and their global spatial distribution.

Large-ensemble experiments by SPEAR_HI

We conducted two types of multidecadal simulation using the SPEAR_HI model: SPEAR_HI_ALL and SPEAR_HI_NAT. A summary of these experiments is provided in Supplementary Table 1. It should be noted that the same experiments were initially conducted using the SPEAR_MED model[9,29], and that this study extended these simulations to SPEAR_HI[30].

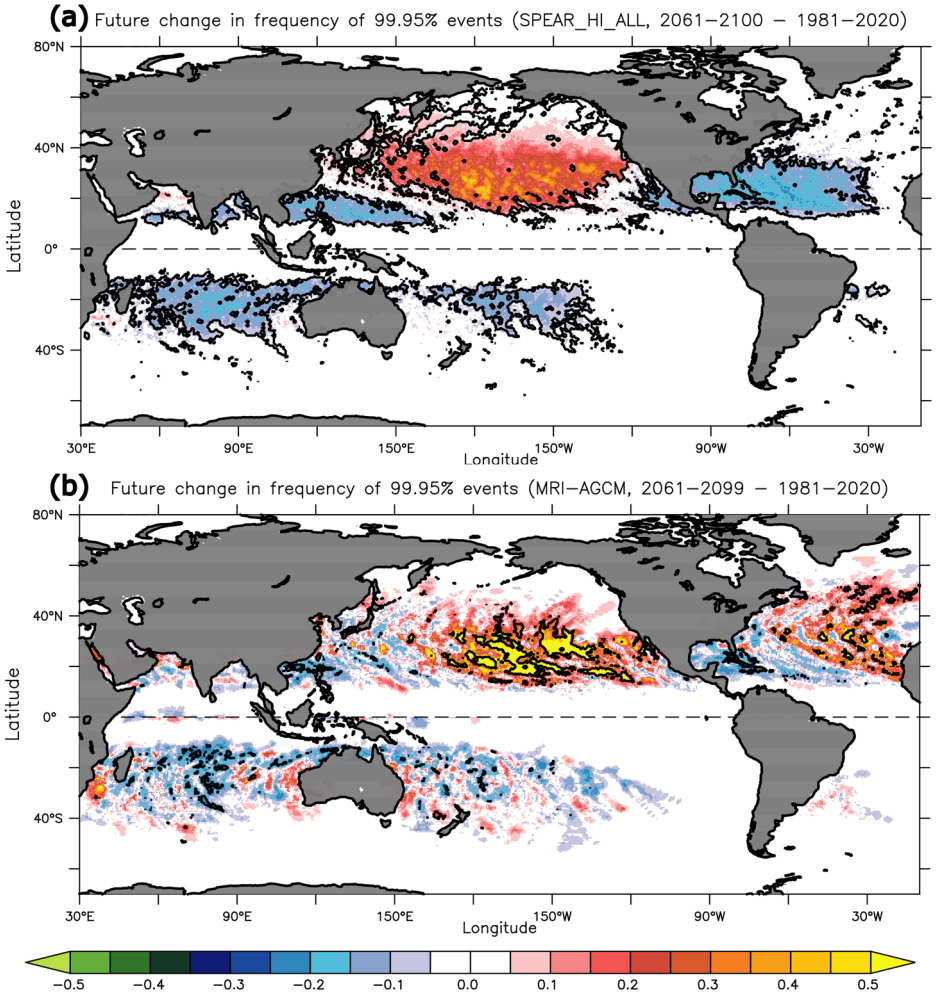

Fig. 5 | Projected changes in the frequency of extreme TSLPG events on a global scale. **a** Projected changes in the mean frequency of 99.95th percentile of TSLPG events only when any TCs (maximum sustained wind speed: ≥17.5 m s^{-1}) simultaneously exist over the grids during the extreme events during 2061–2100 relative to that during 1981–2020 by SPEAR_HI_ALL. **b** As in (**a**), but for MRI-AGCM3.2S. Only peak TC seasons (July–October for the Northern Hemisphere and December–March for the Southern Hemisphere) were considered. Black contours indicate boundaries of the areas of statistically significant changes at the 95% confidence level determined using a bootstrap method.

For the SPEAR_HI_ALL experiments, the historical anthropogenic forcing was prescribed over the historical period 1921–2014, whereas the expected future anthropogenic forcing was prescribed over the period 2015–2100 under the high-emission scenario of Shared Socioeconomic Pathway 5–8.5 (SSP5-85)[45,46]. In the future period, no volcanic events were assumed. We performed ten ensemble simulations for the SPEAR_HI_ALL experiments. The simulations were initiated from restart files derived from 20-year intervals in the long-term preindustrial control experiments such that the simulated internal variability, e.g., the El Niño–Southern Oscillation, was out of phase among the ensemble members.

The experimental settings for SPEAR_HI_NAT were identical to SPEAR_HI_ALL, except that the anthropogenic forcing such as greenhouse gases, anthropogenic aerosols, and ozone were fixed at their 1921 levels. The primary difference between SPEAR_HI_ALL and SPEAR_HI_NAT was the anthropogenic forcing. We conducted six ensemble simulations for SPEAR_HI_NAT due to limited computational resource availability.

Historical and future experiments by MRI-AGCM3.2S

We used MRI-AGCM3.2S to conduct a long-term consecutive historical and future Representative Concentration Pathway 8.5 (RCP8.5) experiment from 1950–2099[32] (as outlined in Supplementary Table 1). Because MRI-AGCM3.2S is an atmospheric model, reference sea surface temperatures (SSTs) and sea ice concentrations (SICs) were prescribed as the lower boundary conditions. During the historical period (1950–2014), observed monthly mean SST and SIC data were prescribed from the Hadley Center Global Sea Ice and Sea Surface Temperature (HadISST1) dataset[47]. For the future period (2015–2099), projected changes in SSTs and SICs based on the ensemble mean of multiple CMIP5 models under the Representative Concentration Pathway 8.5 (RCP8.5) scenario were added to the observed climatological mean SSTs, following the HighResMIP experiment protocol[22,23]. To retain the historical interannual variations of SST and SIC in the future period, detrended interannual variations in observed SSTs and SICs were added to the future mean SSTs and SICs (for additional details, see ref. 48). There was only a single-member experiment for MRI-AGCM3.2S. Note that we ideally aim to include data for 2100, but the future projection for MRI-AGCM3.2S ends in 2099.

TC detection methods

For SPEAR_HI, model-simulated TCs were identified from 6-hourly outputs using the algorithm outlined in refs. 14,49. Briefly, this method applies the flood fill algorithm to identify closed contours of magnitude of SLP anomaly relative to the surrounded mean in conjunction with 3-K temperature anomalies relative to the surrounded mean to detect the warm core of TCs. The storm detection criteria also require a wind speed criterion (17.5 m s^{-1}). These conditions should persist for a minimum of 36 h to eliminate short-lived storms.

For MRI-AGCM3.2S, model-simulated TCs were identified using the approach described in ref. 9. Briefly, this method applies four criteria: relative vorticity at 850 hPa (2.0×10^{-4} s^{-1}), temperature anomaly in the warm core region (2.0 K), maximum wind velocity at 850 hPa (17.0 m s^{-1}), and a minimum duration of 36 h.

Tendency of SLP meridional gradient (TSLPG)

To calculate the tendency of the SLP meridional gradient (TSLPG) near Hawaii, we utilized the 6-hourly SLP anomalies and adopted the following procedure.

Calculation of SLPG. The SLP meridional gradient (SLPG) was computed as the difference in the mean SLP anomalies at two different latitudes (15°N and 25°N) within a longitudinal range of 160–155°W:

$$SLPG = \overline{SLP}^{25^\circ N}_{a_{160-155^\circ W}} - \overline{SLP}^{15^\circ N}_{a_{160-155^\circ W}}, \quad (1)$$

where SLP_a represents the anomaly of 6-hourly SLP relative to the previous 20-year climatological mean. The overbar indicates the mean at the defined latitude within the longitudinal range. These calculations were conducted using the outputs of SLP interpolated onto 0.5° × 0.5° grid cells.

TSLPG Calculation. The TSLPG was then calculated as the rate of change of SLPG over time (t), as follows:

$$TSLPG = \frac{SLPG(t) - SLPG(t - dt)}{dt}, \quad (2)$$

where dt represents a time interval of 24 h.

We computed the TSLPG for all simulated 6-hourly data for July to October, corresponding to the peak TC season in the central Pacific. Subsequently, we determined threshold values for several percentiles (e.g., 90th, 95th, 99th, 99.5th, 99.9th, 99.95th, and 99.99th percentiles) using the TSLPG data for the present-day period of 1981–2020 for reference. These percentile thresholds were used to identify extreme TSLPG events defined when TSLPG exceeded one of these thresholds at a specific time.

Calculations similar to those used for Hawaii were also applied to each grid cell globally. For each grid cell, an area of 10° width latitudinally and a 5° width longitudinally, centered on the grid cell, was applied to compute the TSLPG. The sign of the TSLPG was reversed for grid cells in the Southern Hemisphere, given the reversed spatial structure of the SLP anomalies compared to that in the Northern Hemisphere. As for the Hawaii region, percentile thresholds for each grid cell were calculated using the data of the present-day period (1981–2020). These calculations were conducted for July to October for the Northern Hemisphere and December to March for the Southern Hemisphere to account for the peak TC season.

Statistical significance tests

To evaluate the statistical significance of differences between the mean values of the present-day and the future climates, we utilized the bootstrap method. Following ref. 9, we resampled the data 2000 times with replacements. The same resampling process was employed to obtain the confidence interval.

Data availability

The observed TC data (IBTrACS) are publicly available at https://www.ncdc.noaa.gov/ibtracs/. The observed SST data (HadISST1.1) are available at https://www.metoffice.gov.uk/hadobs/hadisst/. The reanalysis datasets are available at https://climatedataguide.ucar.edu/climate-data/climate-forecast-system-reanalysis-cfsr for CFSR and https://jra.kishou.go.jp/JRA-55/index_en.html for JRA-55. The model outputs by MRI-AGCM3.2S are available online at http://search.diasjp.net/en/dataset/GCM20_SOUSEI. The datasets analyzed during the current study are available at https://doi.org/10.7910/DVN/VAG7LT. These uploaded files are freely available.

Received: 3 January 2024; Accepted: 21 August 2024;
Published online: 02 September 2024

References

1. NOAA National Centers for Environmental Information (NCEI) U.S. Billion-Dollar Weather and Climate Disasters https://doi.org/10.25921/stkw-7w73 (2023).
2. Simpson, R. H. The hurricane disaster potential scale. *Weatherwise* **27**, 169–186 (1974).
3. WMO. WMO Atlas of mortality and economic losses from weather, climate and water extremes (1970-2019) 90 pp. (World Meteorological Organization, 2021).
4. Murakami, H., Levin, E., Delworth, T. L., Gudgel, R. & Hsu, P.-C. Dominant effect of relative tropical Atlantic warming on major hurricane occurrence. *Science* **362**, 794–799 (2018).
5. Garner, A. J., Kopp, R. E. & Horton, B. P. Evolving tropical cyclone tracks in the North Atlantic in a warming climate. *Earth's Future* **9**, e2021EF002326 (2021).
6. Tran, T. L., Ritchie, E. A., Perkins-Kirkpatrick, S. E., Bui, H. & Luong, T. M. Future changes in tropical cyclone exposure and impacts in Southeast Asia from CMIP6 pseudo-global warming simulations. *Earth's Future* **10**, e2022EF003118 (2022).
7. Murakami, H. & Sugi, M. Effect of model resolution on tropical cyclone climate projections. *SOLA* **6**, 73–76 (2010).
8. Manganello, J. V. et al. Tropical cyclone climatology in a 10-km global atmospheric GCM: toward weather-resolving climate modeling. *J. Climate* **25**, 3867–3893 (2012).
9. Murakami, H. et al. Detected climatic change in global distribution of tropical cyclones. *Proc. Natl Acad. Sci. USA* **117**, 10706–10714 (2020).
10. Knutson, T. et al. Tropical cyclones and climate change assessment: Part II. Projected response to anthropogenic warming. *Bull. Amer. Meteor. Soc.* **101**, E303–E322 (2020).
11. IPCC. in *Climate Change 2021: The Physical Science Basis. Contribution of Working Group I to the Sixth Assessment Report of the Intergovernmental Panel on Climate Change* (eds Masson-Delmotte, V. et al.) 2391 pp. (Cambridge Univ. Press, Cambridge, UK, 2021).
12. Camargo, S. J. et al. An update on the influence of natural climate variability and anthropogenic climate change on tropical cyclones. *Trop. Cyclone Res. Rev.* **12**, 216–239 (2023).
13. Murakami, H. et al. Future changes in tropical cyclone activity projected by the new high-resolution MRI-AGCM. *J. Climate* **25**, 3237–3260 (2012).
14. Murakami, H. et al. Simulation and prediction of Category 4 and 5 hurricanes in the high-resolution GFDL HiFLOR coupled climate model. *J. Climate* **28**, 9058–9079 (2015).
15. Bhatia, K. T., Vecchi, G. A., Murakami, H., Underwood, S. & Kossin, J. Projected response of tropical cyclone intensity and intensification in a global climate model. *J. Climate* **31**, 8281–8303 (2018).
16. Vecchi, G. A. et al. Tropical cyclone sensitivities to CO2 doubling: roles of atmospheric resolution, synoptic variability and background climate changes. *Clim. Dyn.* **53**, 5999–6033 (2019).
17. Murakami, H., Mizuta, R. & Shindo, E. Future changes in tropical cyclone activity projected by multi-physics and multi-SST ensemble experiments using the 60-km-mesh MRI-AGCM. *Clim. Dyn.* **39**, 2569–2584 (2012).
18. Camargo, S. J. Global and regional aspects of tropical cyclone activity in the CMIP5 models. *J. Climate* **26**, 9880–9902 (2013).
19. Murakami, H., Hsu, P.-C., Arakawa, O. & Li, T. Influence of model biases on projected future changes in tropical cyclone frequency of occurrence. *J. Climate* **27**, 2159–2181 (2014).
20. Tory, K. J., Chand, S. S., McBride, J. L., Ye, H. & Dare, R. A. Projected changes in late-twenty-first-century tropical cyclone frequency in 13 coupled climate models from phase 5 of the Coupled Model Intercomparison Project. *J. Climate* **26**, 9946–9959 (2013).
21. Camargo, S. J. et al. Characteristics of model tropical cyclone climatology and the large-scale environment. *J. Climate* **33**, 4463–4487 (2020).
22. Haarsma, R. J. et al. High Resolution Model Intercomparison Project (HighResMIP v1.0) for CMIP6. *Geosci. Model Dev.* **9**, 4185–4208 (2016).

23. Roberts, M. J. et al. Impact of model resolution on tropical cyclone simulation using the HighResMIP–PRIMAVERA multimodel ensemble. *J. Climate* **33**, 2557–2583 (2020).
24. Roberts, M. J. et al. Projected future changes in tropical cyclones using the CMIP6 HighResMIP multimodel ensemble. *Geophys. Res. Lett.* **47**, e2020GL088662 (2020).
25. Voldoire, A. et al. Evaluation of CMIP6 DECK experiments with CNRM-CM6-1. *J. Adv. Model. Earth Syst.* **11**, 2177–2213 (2019).
26. Cherchi, A. et al. Global mean climate and main patterns of variability in the CMCC-CM2 coupled model. *J. Adv. Model. Earth Syst.* **11**, 185–209 (2019).
27. Murakami, H., Delworth, T. L., Cooke, W. F., Kapnick, S. B. & Hsu, P.-C. Increasing frequency of anomalous precipitation events in Japan detected by a deep learning autoencoder. *Earth's Future* **10**, e2021EF002481 (2022).
28. The Los Angeles Times: How a perfect storm of climate and weather led to catastrophic Maui fire. Available online at https://www.latimes.com/environment/story/2023-08-11/how-did-climate-change-influence-catastrophic-hawaii-fire (2023).
29. Delworth, T. L. and coauthors. SPEAR – the next generation GFDL modeling system for seasonal to multidecadal prediction and projection. *J. Adv. Model. Earth Syst.* **12**, e2019MS001895 (2020).
30. Jong, B., Delworth, T. L., Cooke, W., Tseng, K. & Murakami, H. Increases in extreme precipitation over the Northeast United States using high-resolution climate model simulations. *npj Clim. Atmos. Sci.* **6**, 18 (2023).
31. Mizuta, R. et al. Climate simulations using the improved MRI-AGCM with 20-km grid. *J. Meteor. Soc. Japan* **90A**, 235–260 (2012).
32. Mizuta, R. et al. Extreme precipitation in 150-year continuous simulations by 20-km and 60-km AGCMs with dynamical downscaling over Japan by a 20-km regional climate model. *J. Meteor. Soc. Japan* **100**, 523–532 (2022).
33. Murakami, H., Wang, B., Li, T. & Kitoh, A. Projected increase in tropical cyclones near Hawaii. *Nat. Clim. Change* **3**, 749–754 (2013).
34. Yoshida, K. & Itoh, H. Indirect effects of tropical cyclones on heavy rainfall events in Kyushu, Japan, during the Baiu season. *J. Meteorol. Soc. Jpn.* **90**, 377–401 (2012).
35. Hirata, H. & Kawamura, R. Scale interaction between typhoons and the North Pacific subtropical high and associated remote effects during the Baiu/Meiyu season. *J. Geophys. Res. Atmos.* **119**, 5157–5170 (2014).
36. Emanuel, K. Response of global tropical cyclone activity to increasing CO_2: results from downscaling CMIP6 models. *J. Climate* **34**, 57–70 (2021).
37. Lee, C.-Y., Camargo, S. J., Sobel, A. H. & Tippett, M. K. Statistical-dynamical downscaling projections of tropical cyclone activity in a warming climate: two diverging genesis scenarios. *J. Climate* **33**, 4815–4834 (2020).
38. Lee, C.-Y., Sobel, A. H., Camargo, S. J., Tippett, M. K. & Yang, Q. New York state hurricane hazard: history and future projections. *J. Appl. Meteorol. Climatol.* **61**, 613–629 (2022).
39. Kobayashi, S. et al. The JRA-55 reanalysis: general specifications and basic characteristics. *J. Meteor. Soc. Japan* **93**, 5–48 (2015).
40. Saha, S. et al. The NCEP climate forecast system reanalysis. *Bull. Amer. Meteor. Soc.* **91**, 1015–1057 (2010).
41. Knapp, K. R., Kruk, M. C., Levinson, D. H., Diamond, H. J. & Neuman, C. J. The international best track archive for climate stewardship (IBTrACS): unifying tropical cyclone best track data. *Bull. Amer. Meteor. Soc.* **91**, 363–376 (2010).
42. Zhao, M. et al. The GFDL global atmospheric and land model AM4.0/LM4.0 – Part I: simulation characteristics with prescribed SSTs. *J. Adv. Model. Earth Syst.* **10**, 735–769 (2018).
43. Zhao, M. et al. The GFDL global atmospheric and land model AM4.0/LM4.0 – Part II: model description, sensitivity studies, and turning strategies. *J. Adv. Model. Earth Syst.* **10**, 735–769 (2018).
44. Yoshimura, H., Mizuta, R. & Murakami, H. A spectral cumulus parameterization scheme interpolating between two convective updrafts with semi-Lagrangian calculation of transport by compensatory subsidence. *Mon. Wea. Rev.* **143**, 597–621 (2015).
45. Kriegler, E. et al. Fossil-fueled development (SSP5): an energy and resource intensive scenario for the 21st century. *Glob. Environ. Change* **42**, 297–315 (2017).
46. Riahi, K. et al. The Shared Socioeconomic Pathways and their energy, land use, and greenhouse gas emissions implications: an overview. *Glob. Environ. Change* **42**, 153–168 (2017).
47. Rayner, N. A. et al. Global analysis of sea surface temperature, sea ice, and night marine air temperature since the late nineteenth century. *J. Geophys. Res.* **108**, 4407 (2003).
48. Mizuta, R., Y. Adachi, S. Yukimoto, and S. Kusunoki. Estimation of the future distribution of sea surface temperature and sea ice using the CMIP3 multi-model ensemble mean. *Tech. Rep. Meteor. Res. Inst*. http://www.mri-jma.go.jp/Publish/Technical/DATA/VOL_56/56.html (2008).
49. Harris, L. M., Lin, S.-J. & Tu, C. Y. High resolution climate simulations using GFDL HiRAM with a stretched global grid. *J. Climate* **29**, 4293–4314 (2016).

Acknowledgements

The authors thank Drs Leo Donner and Bosong Zhang for their invaluable suggestions and insightful comments. H.M. and S.W. prepared this report under award NA18OAR4320123 from the National Oceanic and Atmospheric Administration, U.S. Department of Commerce. This work was supported by MEXT-Program for The Advanced Studies of Climate Change Projection (SENTAN) Grant Number JPMXD0722680734. P.H. is supported by the National Natural Science Foundation of China (42225502). The statements, findings, conclusions, and recommendations presented in this study are solely those of the authors and do not necessarily represent the views or official positions of the National Oceanic and Atmospheric Administration or the U.S. Department of Commerce.

Author contributions

H.M. designed the study, analyzed the results, and authored the manuscript. W.C. performed the SPEAR simulations. R.M., K.Y., and H.E. conducted the MRI-AGCM3.2S simulations. P.H. and S.W. discussed the framework and results of this study with H.M. All authors provided comments and feedback on the manuscript.

Competing interests

The authors declare no competing interests.

Additional information

Supplementary information The online version contains supplementary material available at https://doi.org/10.1038/s43247-024-01644-9.

Correspondence and requests for materials should be addressed to Hiroyuki Murakami or Pang-Chi Hsu.

Peer review information *Communications Earth & Environment* thanks Andra Garner and the other, anonymous, reviewer(s) for their contribution to the peer review of this work. Primary Handling Editors: Adam Switzer and Joe Aslin. A peer review file is available